

Multi-component chemo-mechanics based on transport relations for the chemical potential

P. Shanthraj^{a,b,*}, C. Liu^{b,*}, A. Akbarian^{b,c}, B. Svendsen^{b,c}, D. Raabe^b

^a*The School of Materials, The University of Manchester, Manchester M1 3BB, UK*

^b*Max-Planck-Institut für Eisenforschung, Max-Planck-Straße 1, 40237 Düsseldorf, Germany*

^c*Material Mechanics, RWTH Aachen University, Schinkelstraße 2, 52062 Aachen, Germany*

Abstract

A chemo-mechanical model for a finite-strain elasto-viscoplastic material containing multiple chemical components is formulated and an efficient numerical implementation is developed to solve the resulting transport relations. The numerical solution relies on inverting the model relations in terms of the chemical potential. In this work, a semi-analytical inversion for a general family of multi-component regular-solution chemical free energy models is derived. This is based on splitting the chemical potential relation into a convex contribution, treated implicitly, and a non-convex contribution, treated explicitly. This results in an expression for the system of transport equations in terms of the chemical potential rather than the concentration as the independent field variable, which is then discretised using a finite element method and solved. The proposed method is benchmarked for the case of a solution undergoing spinodal decomposition and a significant reduction of the numerical cost is demonstrated.

Keywords: Multi-component, Chemo-mechanics, Crystal plasticity

1. Introduction

The main goal of modern materials science is the tailoring of materials, including chemical composition and microstructure, in order to obtain improved properties for present-day sustainable technological development. While there has been a

*Corresponding author

Email addresses: pratheek.shanthraj@manchester.ac.uk (P. Shanthraj),
c.liu@mpie.de (C. Liu)

tremendous growth over recent years in the use of modelling and simulation tools towards this goal (Roters et al., 2019; Liu et al., 2018; Wu et al., 2014; Shanthraj and Zikry, 2012), the realistic prediction of the thermo-chemo-mechanical interactions relevant to industrial processes is a still key development required to enable technological advances in material design, manufacturing and product development. Among several full-field simulation approaches, the phase-field method is well-suited to modelling interface kinetics (Boettinger et al., 2002; Vaithyanathan and Chen, 2002; Moelans et al., 2008; Emmerich, 2008). The phase-field method has been successfully applied to describe many thermo-chemo-mechanical processes including solidification (Nestler and Wheeler, 2000), precipitation (Zhou et al., 2010; Jokisaari et al., 2017; Schwarze et al., 2017), fracture (Schneider et al., 2017; Shanthraj et al., 2016, 2017) and dislocation motion (Mianroodi et al., 2019). Further methodological developments including chemo-mechanical interface modelling and homogenisation have been treated recently in ?.

The use of diffuse-interface models to describe interfacial phenomena dates back to Cahn and Hilliard (1958). The original Cahn-Hilliard (CH) equation was used to model phase separation in binary alloys, but has since been extended to multi-component systems and coupled with microelasticity (Moelans et al., 2008). A critical challenge in simulating the thermodynamics of multi-component chemo-mechanical systems is the numerical approximation of a generally non-convex chemical free energy. Numerous methods have been developed to solve such systems using finite difference (Furihata, 2001), mixed (i.e., concentration and chemical potential treated as independent fields) finite element (Barrett et al., 1999; Gomez and Hughes, 2011), isogeometric (Gomez et al., 2008) and spectral (Zhu et al., 1999) spatial discretisations. In the context of numerical time-integration, the stability, robustness and efficiency of the resulting solution algorithm is sensitive to the non-convexity of the chemical free energy. A successful approach in this regard is the splitting of the chemical free energy into concave and convex components, which are then approximated separately (Elliott and Stuart, 1993; Eyre, 1998). In particular, splitting methods have been applied recently to multi-component, multi-phase CH (Boyer and Minjeaud, 2011; Tavakoli, 2016). In the context of a mixed finite-element-based weak formulation of the classic CH relation, (Gomez and Hughes, 2011) employed a chemical energy splitting approach based on the sign of the fourth-order derivatives of this energy. A recent mixed weak formulation of chemo-mechanics for two-phase, two-component finite-deformation gradient elastic solids based on unconditionally stable, second-order accurate time-integration and Taylor expansion of the non-convex energy

has been given by Sagiya et al. (2016).

More recently, Plapp (2011) and Choudhury and Nestler (2012) have formulated the multi-component transport relations starting from a grand-potential functional. However, these approaches are based on a Legendre transformation, which does not exist for more general non-convex forms of the chemical free energy. In this work, a numerical approach is pursued, where a semi-implicit convex splitting is used to invert the multi-component chemical potential relations, resulting in an analogous expression for component transport in terms of the chemical potential rather than the chemical concentration. This paper is organised as follows: the basic model formulation for a single phase elasto-viscoplastic solid is presented in Section 2, followed by an outline of its numerical implementation in Section 3. In particular, since a dissipation potential exists for the flux-force relations of the current model, the corresponding initial boundary-value problems (IBVP) can be formulated with the help of rate variational methods (Svendsen, 2004; Miehe, 2011, 2014). In Section 4 representative examples are used to benchmark and compare the proposed method with conventional transport relations. A summary is provided in Section 5 along with perspectives for future applications.

2. Model formulation

2.1. Basic relations

Let $\mathcal{B}_0 \subset \mathbb{R}^3$ be a microstructural domain of interest, with boundary $\partial\mathcal{B}_0$. Attention is restricted in this work to the case of a single-phase elasto-viscoplastic solid mixture of M diffusing chemical components. Component diffusion and reaction in the mixture is modeled as usual by the corresponding component mass or number balance relations

$$\dot{c}_m = -\text{Div } \mathbf{j}_m + \sigma_m, \quad \text{for } m = 1, \dots, M, \quad (1)$$

in the mixture in terms of component (mass or number) concentration $0 \leq c_m \leq 1$, the corresponding flux density \mathbf{j}_m , and the corresponding specific supply-rate, σ_m . Assuming the mixture is closed with respect to constituent mass or number, the corresponding sum relations

$$1 = \sum_{m=1}^M c_m, \quad \mathbf{0} = \sum_{m=1}^M \mathbf{j}_m, \quad 0 = \sum_{m=1}^M \sigma_m, \quad (2)$$

and (1) imply $\sum_{m=1}^M \dot{c}_m = 0$.

Besides this, the deformation resulting from an applied loading defines a field $\chi(\mathbf{x}) : \mathbf{x} \in \mathcal{B}_0 \rightarrow \mathbf{y} \in \mathcal{B}$ mapping points \mathbf{x} in the undeformed configuration \mathcal{B}_0 to points \mathbf{y} in the deformed configuration \mathcal{B} . Following Shanthraj et al. (2017), the total deformation gradient, given by $\mathbf{F} = \partial\chi/\partial\mathbf{x} = \nabla\chi$, is multiplicatively decomposed as

$$\mathbf{F} = \mathbf{F}_e \mathbf{F}_c \mathbf{F}_p \quad (3)$$

where \mathbf{F}_p is a lattice preserving isochoric mapping due to plastic deformation, \mathbf{F}_c represents the local deformation due to solute misfit, and \mathbf{F}_e is a mapping to the deformed configuration. In the current approach the stress relaxation due to the component diffusion process is captured through the stress-free deformation gradient, \mathbf{F}_c .

Restricting attention to isothermal and quasi-static processes with no external supplies of momentum or energy, the balance relations for linear momentum, angular momentum, and internal energy, are given by

$$\mathbf{0} = \text{Div } \mathbf{P}, \quad \mathbf{P}^T \mathbf{F} = \mathbf{P} \mathbf{F}^T, \quad \dot{\varepsilon} = \mathbf{P} \cdot \dot{\mathbf{F}}, \quad (4)$$

where, \mathbf{P} is the first Piola-Kirchhoff stress, and ε is the referential internal energy density. As well,

$$\dot{\eta} = \theta^{-1} \delta - \theta^{-1} \text{Div} \sum_{m=1}^M \mu_m \mathbf{j}_m + \theta^{-1} \sum_{m=1}^M \mu_m \sigma_m, \quad (5)$$

holds for the mixture entropy balance (e.g., de Groot and Mazur, 1962, Chapter 2), with δ the mixture dissipation-rate density, θ the absolute temperature, and μ_m the chemical potential of component m .

Combination of (1)-(5) yields the form

$$\delta = \mathbf{P} \cdot \dot{\mathbf{F}} + \sum_{m=1}^{M-1} \mu_{\tilde{m}} \dot{c}_m - \dot{\psi} - \sum_{m=1}^{M-1} \mathbf{j}_m \cdot \nabla \mu_{\tilde{m}} \quad (6)$$

for the mixture dissipation-rate density in terms of $\mu_{\tilde{a}} := \mu_a - \mu_M$, and the mixture free energy density $\psi := \varepsilon - \theta\eta$.

The current model formulation is based on the basic constitutive form

$$\psi(\mathbf{F}, \mathbf{F}_p, \mathbf{F}_c, c_m, \tilde{c}_m, \nabla \tilde{c}_m) = \psi_e(\mathbf{F}, \mathbf{F}_p, \mathbf{F}_c) + \psi_c(c_m, \tilde{c}_m, \nabla \tilde{c}_m), \quad (7)$$

for ψ in terms of elastic, ψ_e , and chemical, ψ_c , parts. A non-local field, \tilde{c}_m for $m = 1, \dots, M-1$, is introduced to weakly enforce any dependence of the energy on chemical inhomogeneity through its gradient $\nabla \tilde{c}_m$ (Ubachs et al., 2004). Modelling \mathbf{P} and $\mu_{\tilde{m}}$ as purely energetic in this work, the constitutive relations

$$\mu_{\tilde{m}} = \partial_{c_m} \psi + \partial_{\mathbf{F}_c} \psi \cdot \partial_{c_m} \mathbf{F}_c, \quad \mathbf{P} = \partial_{\mathbf{F}} \psi \quad (8)$$

hold. Together, (6)-(8) result in the residual form

$$\delta = -\partial_{\mathbf{F}_p} \psi \cdot \dot{\mathbf{F}}_p - \sum_{m=1}^{M-1} \mathbf{j}_m \cdot \nabla \mu_{\tilde{m}} \quad (9)$$

for the dissipation-rate density.

2.2. Energetic constitutive relations

The elastic energy, ψ_e , is modelled here relative to the intermediate configuration by the form

$$\psi_e(\mathbf{F}, \mathbf{F}_p, \mathbf{F}_c) = \frac{1}{2} \mathbf{E}_e \cdot \mathbb{C} \mathbf{E}_e, \quad (10)$$

in terms of the Green-Lagrange strain measure

$$\mathbf{E}_e = \frac{1}{2} \mathbf{F}_c^T (\mathbf{F}_e^T \mathbf{F}_e - \mathbf{I}) \mathbf{F}_c, \quad (11)$$

and anisotropic elastic stiffness \mathbb{C} . The work conjugate second Piola-Kirchhoff stress is given by,

$$\mathbf{S} = \mathbb{C} \mathbf{E}_e. \quad (12)$$

The 1st Piola-Kirchhoff stress tensor, \mathbf{P} , is then related to \mathbf{S} through

$$\mathbf{P} = \mathbf{F}_e \mathbf{F}_c \mathbf{S} \mathbf{F}_p^{-T}. \quad (13)$$

Further details are provided in Roters et al. (2019).

2.2.1. Crystal plasticity

The plastic deformation gradient is given in terms of the plastic velocity gradient, \mathbf{L}_p , by the flow rule

$$\dot{\mathbf{F}}_p = \mathbf{L}_p \mathbf{F}_p \quad (14)$$

where \mathbf{L}_p is work conjugate with the Mandel stress in the plastic configuration,

$$\mathbf{M}_p = -\partial_{\mathbf{F}_p} \psi \mathbf{F}_p^T = (\mathbf{F}_e \mathbf{F}_c)^T \mathbf{F}_e \mathbf{F}_c \mathbf{S} \approx \mathbf{F}_c^T \mathbf{F}_c \mathbf{S}. \quad (15)$$

assuming small elastic strains. A crystal plasticity model is used, where the plastic velocity gradient \mathbf{L}_p is composed of the slip rates $\dot{\gamma}^\alpha$ on crystallographic slip systems, which are indexed by α

$$\mathbf{L}_p = \dot{\mathbf{F}}_p \mathbf{F}_p^{-1} = \sum_{\alpha} \dot{\gamma}^\alpha \mathbf{s}^\alpha \otimes \mathbf{n}^\alpha \quad (16)$$

where \mathbf{s}^α and \mathbf{n}^α are unit vectors along the slip direction and slip plane normal, respectively (Roters et al., 2010; Shanthraj and Zikry, 2011). The slip rates are given by the phenomenological description of Peirce et al. (1983),

$$\dot{\gamma}^\alpha = \dot{\gamma}_0 \left| \frac{\tau^\alpha}{g^\alpha} \right|^n \text{sgn}(\tau^\alpha) \quad (17)$$

in terms of the reference shear rate $\dot{\gamma}_0$, and stress exponent n . The slip resistances on each slip system, g^α , evolve asymptotically towards g_∞ with shear γ^β ($\beta = 1, \dots, 12$) according to the relationship

$$\dot{g}^\alpha = \dot{\gamma}^\beta h_0 \left| 1 - g^\beta/g_\infty \right|^a \text{sgn}(1 - g^\beta/g_\infty) h_{\alpha\beta} \quad (18)$$

with parameters h_0 and a . The interaction between different slip systems is captured by the hardening matrix $h_{\alpha\beta}$.

The plastic dissipation can then be reduced to the simpler slip system based conjugate pair

$$-\partial_{\mathbf{F}_p} \psi \cdot \dot{\mathbf{F}}_p = \sum_{\alpha} \tau^\alpha \dot{\gamma}^\alpha, \quad \text{where} \quad \tau^\alpha = \mathbf{M}_p \cdot (\mathbf{s}^\alpha \otimes \mathbf{n}^\alpha). \quad (19)$$

On this basis, non-negativity of $\dot{\gamma}_0$, g_∞ , h_0 and $h_{\alpha\beta}$ is sufficient to ensure non-negative plastic dissipation.

2.2.2. Multi-component chemo-mechanics

Following Hüter et al. (2018), the solute misfit deformation gradient is given by

$$\mathbf{F}_c = \sum_{m=1}^{M-1} (1 + \nu_m c_m) \mathbf{I} \quad (20)$$

where ν_m is the change in local volume per unit mass or number fraction due to component m in the solid matrix.

The chemical energy, ψ_c , is modelled here using the following regular solution form

$$\begin{aligned} \Omega \psi_c(c_m, \tilde{c}_m, \nabla \tilde{c}_m) = & \sum_{m=1}^{M-1} E_m^{sol} c_m + \sum_{m,n=1}^{M-1} E_{mn}^{int} c_m c_n + R\theta \sum_{m=1}^M c_m \ln c_m \\ & + \frac{1}{2} \sum_{m=1}^{M-1} \alpha_m (c_m - \tilde{c}_m)^2 + \frac{1}{2} \sum_{m=1}^{M-1} \kappa_m |\nabla \tilde{c}_m|^2. \end{aligned} \quad (21)$$

where Ω is the volume of the lattice unit cell; E_m^{sol} , κ_m and α_m are respectively the solution energy, gradient coefficient, and penalty parameter to weakly enforce $c_m = \tilde{c}_m$, for component m ; E_{mn}^{int} is the interaction energy between component m and n ; and R is the universal gas constant. The non-local field, \tilde{c}_m , is obtained through the equilibrium relation,

$$\begin{aligned} 0 = -\Omega \partial_{\tilde{c}_m} \psi = & \Omega (\partial_{\tilde{c}_m} \psi - \text{Div } \partial_{\nabla \tilde{c}_m} \psi) \\ = & \alpha_m (\tilde{c}_m - c_m) - \text{Div } \kappa_m \nabla \tilde{c}_m + \alpha_m (c_m - \tilde{c}_m). \end{aligned} \quad (22)$$

A linear flux-force form is assumed for the component diffusion,

$$\mathbf{j}_m = -\mathbf{M}_m \nabla \mu_{\tilde{m}}, \quad (23)$$

with \mathbf{M}_m the component mobility, and chemical potential, $\mu_{\tilde{m}}$, given by

$$\Omega \mu_{\tilde{m}} = E_m^{sol} + \sum_{n=1}^{M-1} E_{mn}^{int} c_n + R\theta \ln \frac{c_m}{c_M} + \alpha_m (c_m - \tilde{c}_m) - \Omega \nu_m (\mathbf{F}_c^T \mathbf{S}) \cdot \mathbf{I}. \quad (24)$$

On this basis, non-negativity of \mathbf{M}_m is sufficient to ensure non-negative dissipation due to component diffusion.

3. Numerical methods

The following represents a special case of the variational treatment of combined Cahn-Hilliard and Allen-Cahn modelling of finite-deformation gradient elastic solids in Gladkov and Svendsen (2015).

As detailed in Svendsen (2004), a rate-variational-based formulation of the IBVPs is contingent in particular on the existence of a dissipation potential for the model in question. In the current case, the force-based form

$$d = \frac{1}{n+1} \sum_{\alpha} g^{\alpha} \dot{\gamma}_0 \left| \frac{\tau^{\alpha}}{g^{\alpha}} \right|^{n+1} + \frac{1}{2} \sum_{m=1}^{M-1} \nabla \mu_{\tilde{m}} \cdot \mathbf{M}_m \nabla \mu_{\tilde{m}}, \quad (25)$$

of this potential determines the fluxes $\dot{\gamma}^\alpha = \partial_{\tau_\alpha} d$ and $\mathbf{j}_m = -\partial_{\nabla \mu_{\tilde{m}}} d$, consistent with (17) and (23), respectively. The convexity of d in the forces, and its non-negativity $d \geq 0$, together imply $\delta \geq 0$ in the context of (9). Besides this potential, the rate-variational formulation is based on the energy storage-rate density, ζ , and the supply rate density, p_s . For the current model, this is given by

$$\zeta := \sum_{m=1}^{M-1} (\mu_{\tilde{m}} \dot{c}_m + \partial_{\tilde{c}_m} \psi \dot{\tilde{c}}_m) + \partial_{\nabla \chi} \psi \cdot \nabla \dot{\chi} - \sum_{\alpha} \tau_{\alpha} \dot{\gamma}_{\alpha}, \quad p_s = \sum_{m=1}^{M-1} \mu_{\tilde{m}} \sigma_m. \quad (26)$$

Together, these determine the volumetric part of the rate functional

$$P = \int_{\mathcal{B}_0} p_v \, d\mathbf{x} + \int_{\partial \mathcal{B}_0^f} p_f \, d\mathbf{s}, \quad \text{where} \quad p_v = \zeta + d + p_s. \quad (27)$$

The flux boundary conditions on $\partial \mathcal{B}_0^f$ is given by p_f . The first variation of P with respect to $\mu_{\tilde{m}}$, $\dot{\chi}$, $\dot{\tilde{c}}_m$, and τ_{α} takes the form

$$\begin{aligned} \delta P = & \sum_{m=1}^{M-1} \int_{\mathcal{B}_0} \delta_{\mu_{\tilde{m}}} p_v \delta \mu_{\tilde{m}} \, d\mathbf{x} + \sum_{m=1}^{M-1} \int_{\partial \mathcal{B}_0^f} (\partial_{\nabla \mu_{\tilde{m}}} p_v \mathbf{n}_{\partial \mathcal{B}_0} + \partial_{\mu_{\tilde{m}}} p_f) \delta \mu_{\tilde{m}} \, d\mathbf{s} \\ & + \int_{\mathcal{B}_0} \delta_{\dot{\chi}} p_v \delta \dot{\chi} \, d\mathbf{x} + \int_{\partial \mathcal{B}_0^f} (\partial_{\nabla \dot{\chi}} p_v \mathbf{n}_{\partial \mathcal{B}_0} + \partial_{\dot{\chi}} p_f) \delta \dot{\chi} \, d\mathbf{s} \\ & + \sum_{m=1}^{M-1} \int_{\mathcal{B}_0} \partial_{\dot{\tilde{c}}_m} p_v \delta \dot{\tilde{c}}_m \, d\mathbf{x} + \sum_{\alpha} \int_{\mathcal{B}_0} \partial_{\tau_{\alpha}} p_v \delta \tau_{\alpha} \, d\mathbf{x} \end{aligned} \quad (28)$$

via integration by parts and the divergence theorem. Necessary for stationarity, $\delta P = 0$, of (28) are the weak forms for the field relations

$$\begin{aligned} & \int_{\mathcal{B}_0} \partial_{\nabla \chi} \psi \cdot \nabla \delta \dot{\chi} \, d\mathbf{x} - \int_{\partial \mathcal{B}_0} \partial_{\dot{\chi}} p_f \delta \dot{\chi} \, d\mathbf{s} = 0, \\ & \int_{\mathcal{B}_0} [(\dot{c}_m - \sigma) \delta \mu_{\tilde{m}} + \mathbf{M}_m \nabla \mu_{\tilde{m}} \cdot \nabla \delta \mu_{\tilde{m}}] \, d\mathbf{x} = 0, \\ & \int_{\mathcal{B}_0} [\alpha_m (c_m - \tilde{c}_m) \delta \tilde{c}_m + \kappa_m \nabla \tilde{c}_m \cdot \nabla \delta \tilde{c}_m] \, d\mathbf{x} = 0, \end{aligned} \quad (29)$$

and constitutive relation $0 = -\dot{\gamma}^\alpha + \partial_{\tau_{\alpha}} d$.

3.1. Finite element implementation

The rate-variational formulation yields the weak form of the field relations required for their finite-element (FE) implementation. In particular, equation (29) yields directly the weak momentum balance relation

$$\mathbf{0} = \int_{\mathcal{B}_0} \nabla \delta \dot{\boldsymbol{\chi}} \cdot \mathbf{P} d\mathbf{x}, \quad (30)$$

where $p_f = 0$ is assumed for simplicity, the weak multi-component transport relation

$$\int_{\mathcal{B}_0} [(\dot{c}_m - \sigma) \delta \mu_{\tilde{m}} + \mathbf{M}_m \nabla \mu_{\tilde{m}} \cdot \nabla \delta \mu_{\tilde{m}}] d\mathbf{x} = 0, \quad (31)$$

and the weak non-local relation

$$\int_{\mathcal{B}_0} [\alpha_m (c_m - \tilde{c}_m) \delta \tilde{c}_m + \kappa_m \nabla \tilde{c}_m \cdot \nabla \delta \tilde{c}_m] d\mathbf{x} = 0. \quad (32)$$

where $\delta \dot{\boldsymbol{\chi}}$, $\delta \mu_{\tilde{m}}$ and $\delta \tilde{c}_m$ are the virtual deformation rate, chemical potential and non-local concentration fields respectively. No-flux boundary conditions are assumed for the sake of simplicity.

The deformation field, $\boldsymbol{\chi}(\mathbf{x})$, chemical potential, $\mu_{\tilde{m}}(\mathbf{x})$, and non-local concentration field, $\tilde{c}_m(\mathbf{x})$, in addition to their virtual counterparts are discretised using a FE basis of shape functions, N_i^χ , N_i^μ , $N_i^{\tilde{c}}$, $N_i^{\delta \dot{\boldsymbol{\chi}}}$, $N_i^{\delta \mu}$, and $N_i^{\delta \tilde{c}}$, where $[\boldsymbol{\chi}]_i$, $[\mu_{\tilde{m}}]_i$, $[\tilde{c}_m]_i$, $[\delta \dot{\boldsymbol{\chi}}]_i$, $[\delta \mu_{\tilde{m}}]_i$, and $[\delta \tilde{c}_m]_i$ are the respective degrees of freedom. The corresponding discrete differential operator matrices are \mathbf{B}_i^χ , \mathbf{B}_i^μ , $\mathbf{B}_i^{\tilde{c}}$, $\mathbf{B}_i^{\delta \dot{\boldsymbol{\chi}}}$, $\mathbf{B}_i^{\delta \mu}$ and $\mathbf{B}_i^{\delta \tilde{c}}$. Under these approximations, the weak forms equations (30) to (32) can be rewritten as

$$\sum_i [\delta \dot{\boldsymbol{\chi}}]_i^T \underbrace{\int_{\mathcal{B}_0} [\mathbf{B}_i^{\delta \dot{\boldsymbol{\chi}}}]^T \mathbf{P} d\mathbf{x}}_{\mathcal{R}_i^{\text{mech}}} = 0, \quad (33)$$

$$\sum_i [\delta \mu_{\tilde{m}}]_i^T \underbrace{\int_{\mathcal{B}_0} \left[[N_i^{\delta \mu}]^T (\dot{c}_m - \sigma_m) + [\mathbf{B}_i^{\delta \mu}]^T \mathbf{M} \mathbf{B}_i^\mu [\mu_{\tilde{m}}]_i \right] d\mathbf{x}}_{\mathcal{R}_{i,m}^{\text{chem}}} = 0, \quad (34)$$

$$\sum_i [\delta \tilde{c}_m]_i^T \underbrace{\int_{\mathcal{B}_0} \left[[N_i^{\delta \tilde{c}}]^T \alpha_m (c_m - N_i^{\tilde{c}} [\tilde{c}_m]_i) + [\mathbf{B}_i^{\delta \tilde{c}}]^T \kappa_m \mathbf{B}_i^{\tilde{c}} [\tilde{c}_m]_i \right] d\mathbf{x}}_{\mathcal{R}_{i,m}^{\text{NL}}} = 0, \quad (35)$$

which defines a non-linear system of equations for the unknowns $[\chi]_i$, $[\mu_{\tilde{m}}]_i$, and $[\tilde{c}_m]_i$. A time-discrete system of equations is obtained by using a backward Euler approximation

$$\dot{c}_m = \frac{c_m(t_n) - c_m(t_{n-1})}{\Delta t} \quad (36)$$

of the rate \dot{c}_m in equation (34).

The solution approach followed in this work involves solving the coupled system of equations (33) to (35) within a staggered iterative loop until a self consistent solution is achieved for a time increment.

3.2. Chemical potential solution

Implicit to the solution of the coupled system of equations (33) to (35), with the deformation field, χ , chemical potential, $\mu_{\tilde{m}}$, and non-local concentration field, \tilde{c}_m as primary field variables, is an inversion of the chemical potential equation (24), *i.e.* expressing $c_m := c_m(\mu_{\tilde{m}})$ for $m, n = 1, \dots, M - 1$. This is achieved algorithmically in the current work through a semi-implicit splitting of the chemical potential relation,

$$\mu_{\tilde{m}}(t_n) = \check{\mu}_{\tilde{m}}(t_n) + \hat{\mu}_{\tilde{m}}(t_{n-1}), \quad (37)$$

into a convex

$$\Omega \check{\mu}_{\tilde{m}}(t_n) = E_m^{sol} + R\theta \ln \frac{c_m(t_n)}{c_M(t_n)} + \alpha_m (c_m(t_n) - \tilde{c}_m) - \Omega \nu_m (\mathbf{F}_c^T \mathbf{S}) \cdot \mathbf{I}, \quad (38)$$

and non-convex, *i.e.*,

$$\Omega \hat{\mu}_{\tilde{m}}(t_{n-1}) = \sum_{n=1}^{M-1} E_{mn}^{int} c_n(t_{n-1}), \quad (39)$$

part. Equation (38) can then be inverted to express $c_m(t_n)$ in terms of equations (37) and (39), yielding,

$$c_m(t_n) = \frac{\exp\left(\frac{f_m - \alpha_m c_m(t_n)}{R\theta}\right)}{1 + \sum_{n=1}^{M-1} \exp\left(\frac{f_n - \alpha_n c_n(t_n)}{R\theta}\right)}, \quad (40)$$

where

$$f_m = \Omega \mu_{\tilde{m}}(t_n) - E_m^{sol} + \alpha_m \tilde{c}_m + \Omega \nu_m (\mathbf{F}_c^T \mathbf{S}) \cdot \mathbf{I}. \quad (41)$$

Equation (40) is an implicit system of equations to be numerically solved for $c_m(t_n)$ for a given set $\mu_{\tilde{n}}(t_n)$. A fixed point iteration is employed, which is unconditionally convergent for $\alpha_m \geq 0$ as the norm of the fixed point operator, *i.e.* the RHS in equation (40), is guaranteed to be less than 1.

4. Results and discussion

In this section, the performance of the developed chemo-mechanical model for multi-component finite-strain elasto-viscoplastic materials is validated and benchmarked.

4.1. Validation and benchmarking of the numerical scheme

Diffusion simulations are first performed to study the convergence, accuracy and performance of the proposed numerical scheme for the CH model.

4.1.1. Convergence behaviour

A non-local concentration field, \tilde{c} , is introduced in the current model to account for the gradient energy contributions, thereby reducing the strong fourth-order CH PDE to two weakly non-local second-order PDEs. The conditions which should be fulfilled for the proposed method to approach the results by the strong CH solution are discussed in this section. To investigate the effect of the penalty parameter and the gradient coefficient on the equilibrium numerical solution, we study one-dimensional diffusion simulations without mechanical deformation. Parameters for the chemical free energy density function in equation (21) are taken as $\Omega = 1 \times 10^{-5} \text{m}^3 \text{mol}^{-1}$, $E_1^{sol} = 1.24 \times 10^4 \text{Jmol}^{-1}$, $E_{11}^{int} = -1.24 \times 10^4 \text{Jmol}^{-1}$, $\theta = 498 \text{K}$, $\kappa_1 = 1 \times 10^{-16} \text{Jm}^{-2} \text{mol}^{-1}$, $\mathbf{M}_m = 2.2 \times 10^{-19} \text{m}^2 \text{s}^{-1} \text{J}^{-1}$ and the penalty parameter α_1 varies from 4×10^3 to $2.5 \times 10^6 \text{Jmol}^{-1}$. The resulting equilibrium concentrations for the two coexisting phases are $c_\alpha = 0.07$ and $c_\beta = 0.93$, respectively. The chemical free energy without mechanical deformation of the studied system is shown as the black curve in figure 1. The binodal concentrations in the double-well free energy curve represent the two separated equilibrium phases formed from the initial homogeneous mixture.

The one-dimensional model contains two initial unstable phases with a stepwise change of concentration in the middle of the model. The initial concentrations for these two phases are taken as 0.49 and 0.51, respectively. The system size is $3 \mu\text{m}$ and meshed with 300 regular hexahedral elements.

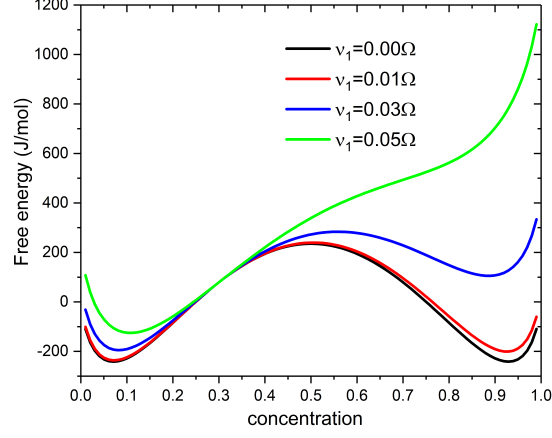


Figure 1: Influence mismatch strain coefficient on the free energy for $\nu_1 = 0.01, 0.03$, and 0.05Ω . Note that in this plot, it is assumed that the solute strain can only be accommodated by the elastic deformation.

Figure 2(a) shows the maximum of the absolute value of difference between concentration and non-local concentration, $\max|c - \tilde{c}|$, at steady state, with increasing values of the penalty parameter. One can clearly observe that the difference, $\max|c - \tilde{c}|$, decreases substantially from 0.34 to 1.7×10^{-2} with increasing the penalty parameter from 4×10^3 to $1.0 \times 10^5 \text{Jmol}^{-1}$. After that the difference, $\max|c - \tilde{c}|$, tends to zero with increasing penalty parameter up to $2.5 \times 10^6 \text{Jmol}^{-1}$. The relation between the difference, $\max|c - \tilde{c}|$, and the penalty parameter on a log-log scale is also given in figure 2(a). It can be seen that the difference, $\max|c - \tilde{c}|$, and the penalty parameter exhibit an exponential relationship, and the difference, $\max|c - \tilde{c}|$, decreases to a relatively low value of 6.8×10^{-4} for a large penalty parameter of $2.5 \times 10^6 \text{Jmol}^{-1}$. Figure 2(b) presents the variation of the interface width, d , with increasing the penalty parameter. The results clearly shows that the interface width converges to a constant value of $4.3 \times 10^{-7} \text{m}$ when the penalty parameter is larger than $1.0 \times 10^5 \text{Jmol}^{-1}$. It also suggests that the convergence of the interface width could be the indicator for choosing an appropriate penalty parameter.

An alternative way to measure the convergence of the proposed numerical algorithm is to characterize the relationship between the gradient coefficient, κ_m , and the interface width, d . Based on the classical CH theory analysis (Cahn and

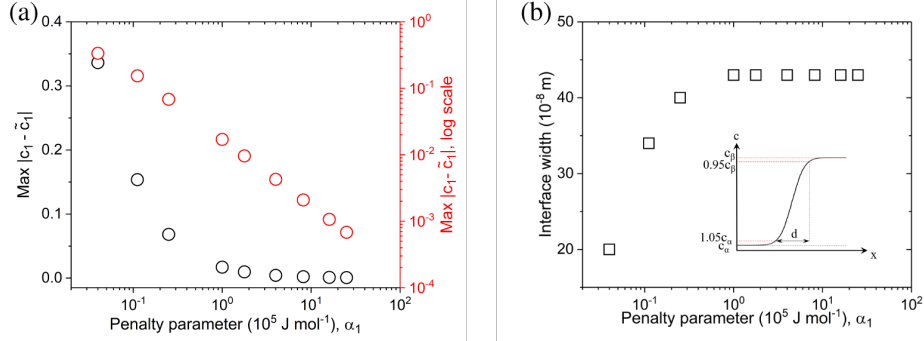


Figure 2: (a) Convergence of the difference, $\max|c - \tilde{c}|$, as a function of the penalty parameter (α_1 , 4×10^3 to $2.5 \times 10^6 \text{ Jmol}^{-1}$). The relationship between the $\max|c - \tilde{c}|$ and α_1 is also given in a log-log scale (red circles). (b) Relationship between the interface width and the penalty parameter (α_1 , 4×10^3 to $2.5 \times 10^6 \text{ Jmol}^{-1}$) at a constant gradient coefficient $\kappa_1 = 1 \times 10^{-16} \text{ Jmol}^{-1} \text{ m}^{-2}$. Schematic of the phase interface between binodal concentration c_α and c_β is given in the inset. The interface width d is defined as the distance where the concentration changes from $1.05c_\alpha$ to $0.95c_\beta$.

Hilliard, 1958), the gradient coefficient should have linear relationship with the interface width squared. Figure 3 shows the simulated interface width squared as a function of the gradient coefficient at steady state. The gradient coefficient κ_1 varies from 1×10^{-17} to $1 \times 10^{-15} \text{ Jmol}^{-1} \text{ m}^{-2}$. Note that for each simulation, the penalty parameter is chosen large enough to guarantee that the interface width converges to the constant value as discussed above. Figure 3 clearly presents the linear relationship between the simulated interface width and the gradient coefficient except the slight deviation at only very few points. Hence, the interface width solely depends on the relative magnitude of the chemical free energy and the interface gradient energy. The penalty parameter does not affect the simulation results as expected when it takes a relatively large value. The above results indicate that the numerical solutions should approach to those obtained from the conventional CH model when the penalty parameter is sufficiently large.

4.1.2. Numerical performance

In this section, the accuracy and performance of the proposed inverted formulation is compared to a conventional CH solution scheme. A two-dimensional numerical example in the absence of mechanical deformation is solved to compare the two solution schemes. The model parameters used are as following: $\Omega = 1 \times 10^{-5} \text{ m}^3 \text{ mol}^{-1}$, $E_1^{sol} = 2 \times 10^4 \text{ Jmol}^{-1}$, $E_{11}^{int} = -5 \times 10^4 \text{ Jmol}^{-1}$, $R\theta =$

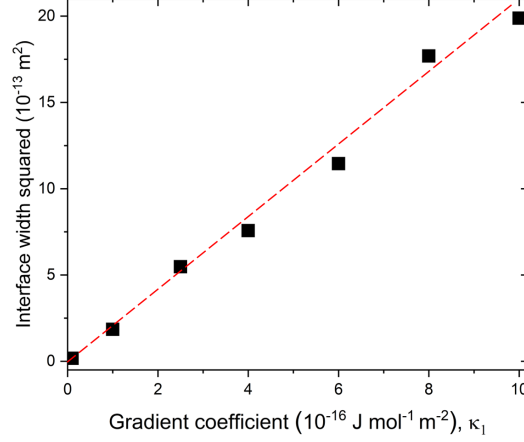


Figure 3: Interface width squared as a function of the gradient coefficient (κ_1 , from 1×10^{-17} to $1 \times 10^{-15} \text{Jmol}^{-1} \text{m}^{-2}$) obtained from simulations (dark squares) and compared with the ideal Cahn-Hilliard scaling (red line).

$0.1 \times 10^4 \text{Jmol}^{-1}$, $\kappa_1 = 1 \times 10^{-16} \text{Jm}^{-2} \text{mol}^{-1}$, $M_m = 1.0 \times 10^{-19} \text{m}^2 \text{s}^{-1} \text{J}^{-1}$, $\alpha_1 = 5 \times 10^5 \text{Jmol}^{-1}$, which results in two equilibrium phases with concentrations of 1.0×10^{-4} and 9.9×10^{-1} , respectively. The initial chemical concentration is taken as 0.5 with a maximum random perturbation of 0.1.

Figure 4 shows the simulated temporal evolution during phase separation of a homogeneous mixture into two equilibrium phases. The unknown field in the numerical implementations is concentration and chemical potential, respectively. The results clearly present that the simulated phase separation and coarsening results are the same for these two different numerical implementations. In order to quantitatively compare the simulation results obtained from the conventional direct transport equation and the proposed inverted transport relation, figure 5 shows the evolution of the maximum and minimum values of the concentration during the spinodal decomposition process, with phase separation initiating at 500s. It can be seen that the simulated results for these two different approaches completely overlap during the entire phase evolution process. Therefore, the above simulations have confirmed the accuracy of the proposed numerical approach.

In order to compare the numerical performance of the two numerical approaches, the same Newton-Raphson scheme is used in the above simulations. The number of iterations required to obtain the solution for the nonlinear Newton-Raphson

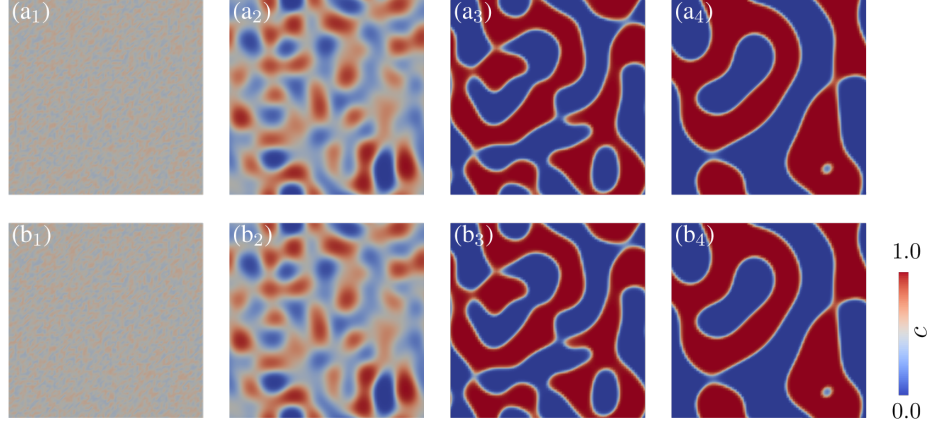


Figure 4: The evolution of phase separation from a homogeneous mixture into two equilibrium phases at different times of 1s, 500s, 1000s, and 1800s. The numerical implementations of the transport relations is based on (a) concentration and (b) chemical potential, respectively.

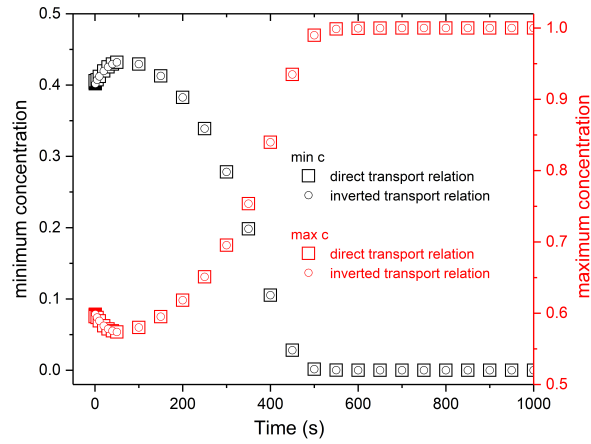


Figure 5: Evolution of the maximum (red) and minimum (black) values of the concentration during the spinodal decomposition process obtained from direct (squares) and inverted (circles) numerical approaches, respectively.

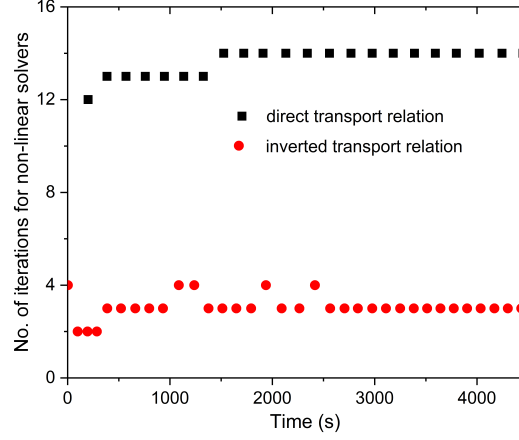


Figure 6: Number of Newton iterations required to solve each time step during the simulation process for the direct (black squares) and inverted (red circles) transport relations.

solver at each time step is used to quantify the performance and efficiency of the numerical scheme. The number of Newton iterations for both approaches during the calculations is shown in figure 6. The number of Newton iterations for solving the inverted transport relations (2-4) is significantly lower than that for solving the conventional transport relations (12-14). These comparisons evidently verified the high performance and the enhanced efficiency of the proposed numerical scheme by inverting the transport relations in terms of the chemical potential rather than the concentration.

4.2. Chemo-mechanical coupling

In this section, the chemical diffusion model is coupled to a finite-strain mechanical model to study the role of mechanical deformation on the diffusion controlled phase separation and coarsening process. Both elastic and plastic deformation accompanying diffusion are considered in the simulations. The material parameters for the chemical energy and crystal plasticity model are listed in table 1. To intuitively demonstrate how the mechanical deformation, through the solute strain F_c in equation (20), affects the free energy of the system, figure 1 shows the free energy of a one-dimensional system with various values of the mismatch strain coefficient. Note that in this plot, it is assumed that the solute strain can only be accommodated by elastic deformation. It can be seen that in terms of kinetics, the

driving force for phase separation decreases with increasing levels of the solute strain. From an energetic point of view, the miscibility gap reduces the equilibrium concentrations for the two separated phases are modified.

Table 1: Chemo-mechanical material parameters for the binary spinodal system

Chemical energy	Ω (m ³ mol ⁻¹)	E_1^{sol} (Jmol ⁻¹)	E_{11}^{int} (Jmol ⁻¹)	θ (K)	
	1×10^{-5}	1.24×10^4	-1.24×10^4	498	
	κ_1 (Jm ⁻² mol ⁻¹)	α_1 (Jmol ⁻¹)	M_1 (m ² s ⁻¹ J ⁻¹)		
	2.5×10^{-17}	5×10^5	2.2×10^{-19}		
Crystal plasticity model	$\dot{\gamma}_0$ (s ⁻¹)	n	g_0 (MPa)	g_∞ (MPa)	a
	1×10^{-3}	20	31	63	2.25
	h_0 (MPa)	Coplanar $h_{\alpha\beta}$ (MPa)	Non-coplanar $h_{\alpha\beta}$ (MPa)		
	75	1	1.4		
Elastic constants	C_{11} (Pa)	C_{12} (Pa)	C_{44} (Pa)		
	1.06×10^{11}	6.0×10^{10}	2.8×10^{10}		

A square domain with an edge length of 2.56 μm and meshed with 256×256 regular hexahedral elements has been modelled. Periodic boundary conditions on both concentrations and displacements were applied on all the boundaries. Figure 7 illustrates the phase evolution process in the reference simulation in the absence of mechanical deformation. At the early stage of the spinodal decomposition, the initial homogeneous mixture simultaneously separates to two phases with equilibrium concentrations. The phase separation stage is driven by the minimization of chemical free energy. Following separation, coarsening can be observed from figure 7, which is driven by the minimization of interface energy, which occurs at a longer time scale compared to the initial phase separation stage.

We then study the effect of the solute strain on the phase separation and coarsening. We first consider the case of an elastically deforming material. The mismatch strain coefficient is taken as $\nu_1 = 0.01, 0.03$, and 0.05Ω , respectively, and the material parameters used are listed in table 1. The simulated temporal evolution of the phases during spinodal decomposition considering elastic deformation is shown in figure 8. It can be seen that the phase evolution is slightly affected when the solute induced strain is relatively small ($\nu_1 = 0.01\Omega$), comparing figure 7 and figure 8(a). However, as the mismatch strain coefficient increases, the phase separation kinetics are significantly slowed, as shown in figure 8(b and c), as the

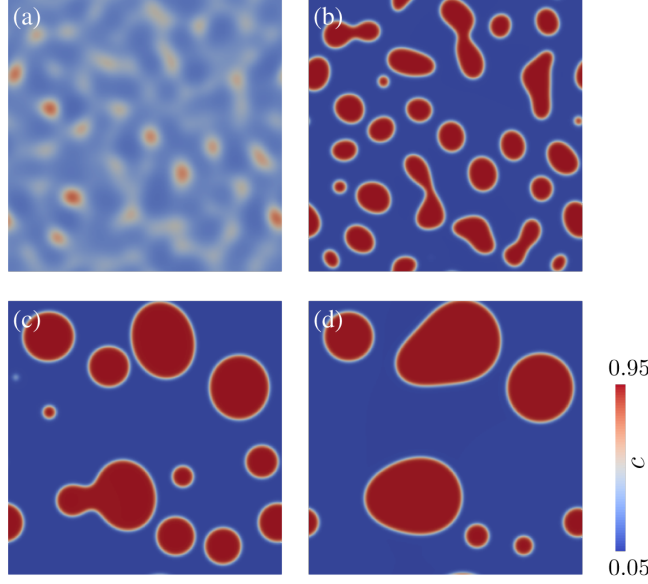


Figure 7: Phase separation and coarsening in the absence of mismatch solute strain at (a) 500s, (b) 800s, (c) 6000s, and (d) 10000s.

increasing elastic energy reduces the driving force for phase separation (figure 1). The equilibrium concentrations for the two separated phases are also affected by the chemo-mechanical coupling. The equilibrium concentration for the solute-rich phase decreases from 0.93 to 0.82 when the mismatch strain increases to 0.05. Furthermore, one can observe that the morphology of the phases is also affected by the solute strain, comparing figure 7 and figure 8(c). The solute-rich phase in the absence of mechanical coupling exhibit a droplet morphology due to the isotropic nature of the interface energy. However, the morphology of the solute-rich phase orders itself along the softer directions of the cubically anisotropic elastic stiffness tensor used here.

To our knowledge, the numerical investigations presented in the literature are limited to the coupling of elastic deformation with diffusion. There are few references reporting numerical simulations of the CH model coupled with elasto-vicoplastic deformation. The capability of the developed chemo-mechanical model allows us to explore the important influence of plasticity on the spinodal decomposition and coarsening, which is observed in materials applications such as rafting in superalloys (Kontis et al., 2018) and hydride formation (Korbmacher et al., 2018). Parameters used for the crystal plasticity model are listed in table 1.

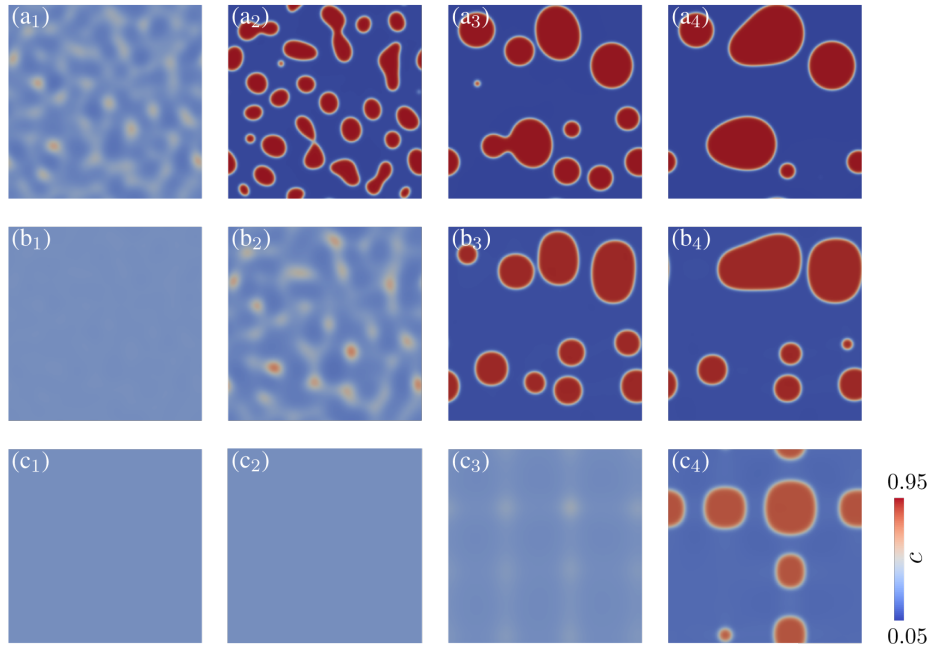


Figure 8: Phase separation and coarsening considering elastic deformation with mismatch strain coefficient, (a) $\nu_1 = 0.01\Omega$, (b) $\nu_1 = 0.03\Omega$, and (c) $\nu_1 = 0.05\Omega$, at time (1) 500s, (2) 800s, (3) 6000s, and (4) 10000s.

The simulated temporal evolution of the phases during spinodal decomposition considering elastic-plastic deformation is shown in figure 9. Comparing figure 8 and figure 9, it can be clearly observe that plastic deformation substantially affects the phase evolution by relaxing shear stresses. Phase separation is observed at 6000s in the plastic material compared to 10000s in the elastic material, for the largest mismatch strain coefficient considered. In addition, the equilibrium concentrations of the two phases with plasticity are close to those obtained from the simulations in the absence of mechanical deformation, since the solute strain induced stress can be effectively relaxed by the plastic deformation.

Figure 10 presents the evolution of the hydrostatic stress and plastic shear distribution for the cases with only elastic and elastic-plastic deformation at a mismatch strain coefficient of 0.03. It can be seen that the plastic deformation substantially relaxes the hydrostatic stress generated due to the phase separation and thus dissipates a significant portion of the stored elastic energy. The plastic strain concentrates around the shell of the phases, with a maximum value of 0.6. More interestingly, even though the equilibrium concentrations of the phases are similar to the case without mechanical deformation, the morphology of the solute-rich phase differs significantly. When considering plastic deformation, the solute-rich phase exhibits elliptic morphology at the medium solute strain, as shown in figure 9(b). At the high solute strain case, the solute-rich phases merge together and multiple strip-like phases can be observed, as shown in figure 9(c).

4.3. Ternary chemo-mechanical spinodal decomposition

In order to illustrate the capability of the modelling approach in the practical engineering applications, a large three-dimensional (3D) simulation of a chemo-mechanically coupled ternary spinodal decomposition and coarsening process is considered. The cubic domain with an edge length of $1.28\ \mu\text{m}$ and meshed with $128 \times 128 \times 128$ regular hexahedral elements has been modelled. The initial concentrations for solute A and B are 0.3 and 0.3, respectively, with a maximum random perturbation of 0.01. The chemical free energy parameters listed in table 2, and material parameters of crystal plasticity material parameters are listed in table 1. The chemical free energy parameters used will result in the formation of three different equilibrium phases: (A-rich, B-poor), (A-poor, B-rich), and (A-poor, B-poor).

Figure 11 shows the temporal evolution of the morphologies of different phases, the accompanying hydrostatic stress, and the plastic shear deformation. In this 3D ternary spinodal decomposition simulation, the separated phases exhibit inter-

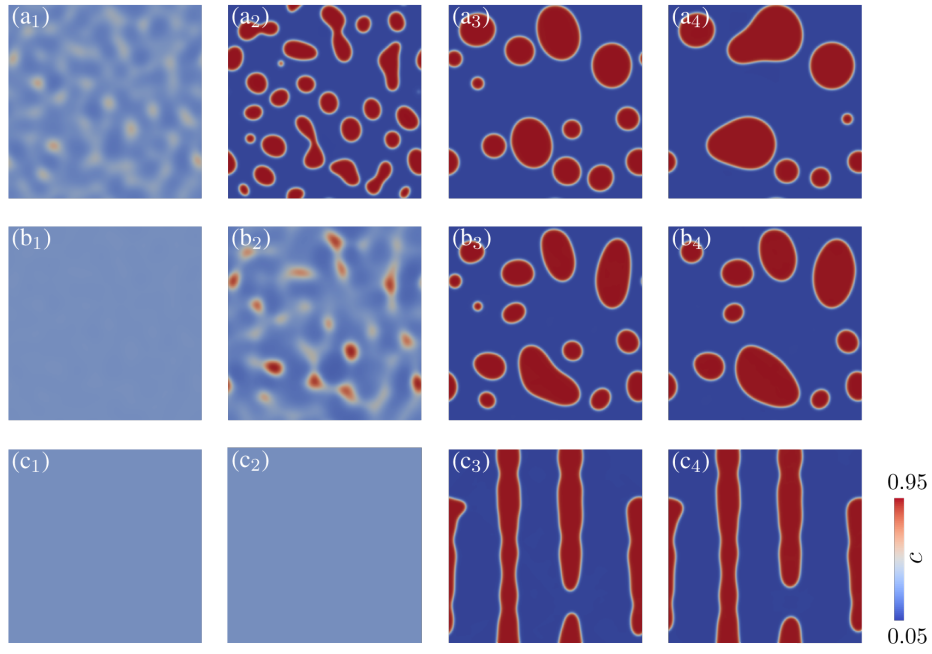


Figure 9: Phase separation and coarsening considering elasto-viscoplastic deformation with mismatch strain coefficient, (a) $\nu_1 = 0.01\Omega$, (b) $\nu_1 = 0.03\Omega$, and (c) $\nu_1 = 0.05\Omega$, at time (1) 500s, (2) 800s, (3) 6000s, and (4) 10000s.

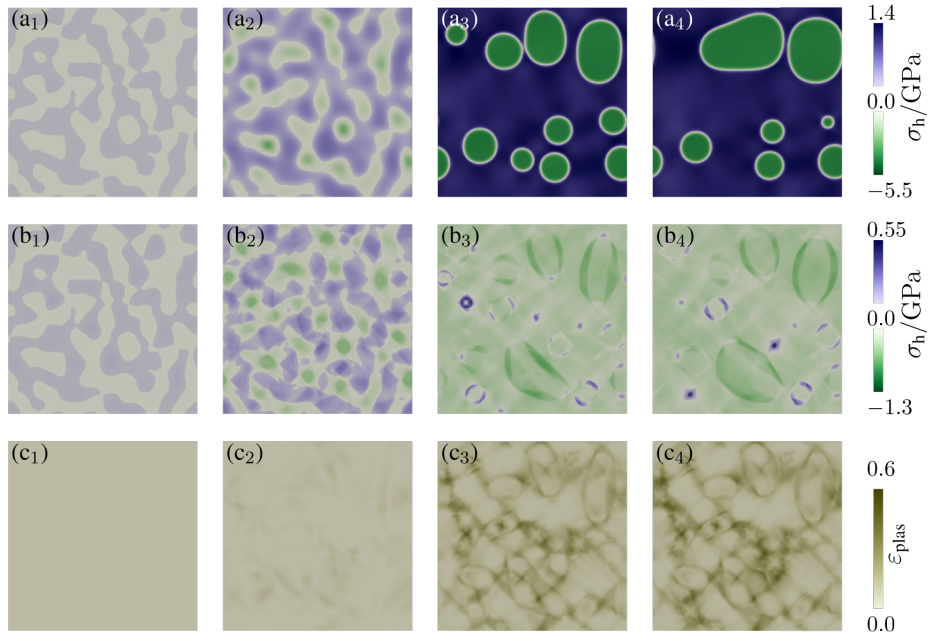


Figure 10: Evolution of the hydrostatic stress accompanying spinodal decomposition (a) without and (b) with plasticity, at a mismatch strain coefficient of $\nu_1 = 0.03\Omega$, at time (1) 500s, (2) 800s, (3) 6000s, and (4) 10000s, and (c) the corresponding evolution of the plastic shear deformation.

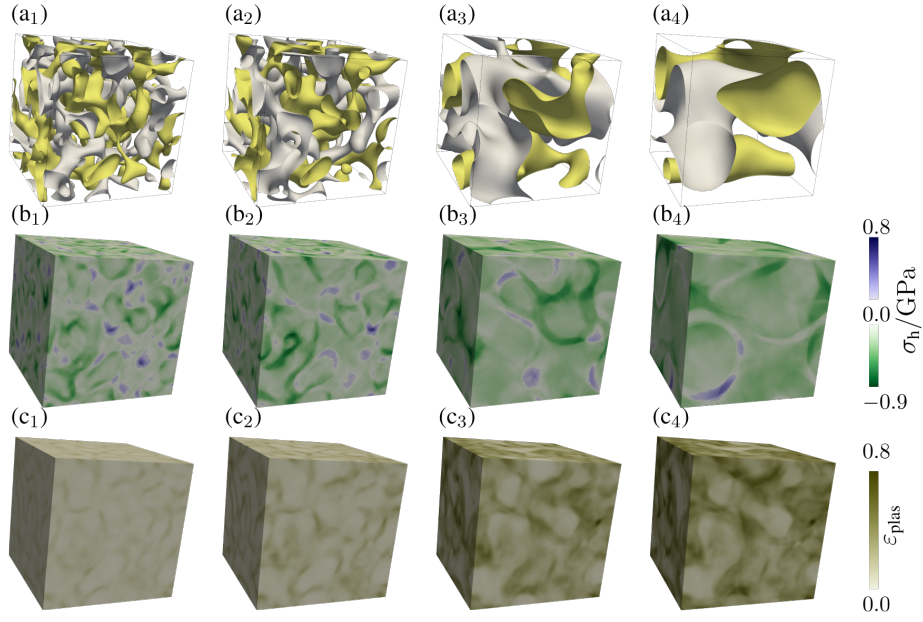


Figure 11: Evolution of (a) phases morphologies, (b) the hydrostatic stress, and (c) the plastic shear deformation in a ternary spinodal decomposition and coarsening process, considering elasto-plastic deformation, with a mismatch strain coefficient of $\nu_1 = 0.03\Omega$, at time (1) 400s, (2) 1000s, (3) 6000s, and (4) 15000s. The grey and yellow iso-surfaces represent (A-rich, B-poor) and (A-poor, B-rich) phases respectively, and the rest is (A-poor, B-poor) matrix phase. The concentrations of the iso-surfaces for both solute A and B are taken as 0.9.

Table 2: Chemical free energy parameters for the ternary spinodal system

Parameter	Value	Parameter	Value
Ω	$1 \times 10^{-5} \text{ (m}^3\text{mol}^{-1}\text{)}$	κ_A	$1 \times 10^{-18} \text{ (Jm}^{-2}\text{mol}^{-1}\text{)}$
E_A^{sol}	$1.24 \times 10^4 \text{ (Jmol}^{-1}\text{)}$	κ_B	$1 \times 10^{-18} \text{ (Jm}^{-2}\text{mol}^{-1}\text{)}$
E_B^{sol}	$1.24 \times 10^4 \text{ (Jmol}^{-1}\text{)}$	α_A	$1 \times 10^5 \text{ (Jmol}^{-1}\text{)}$
E_{AA}^{int}	$-1.24 \times 10^4 \text{ (Jmol}^{-1}\text{)}$	α_B	$1 \times 10^5 \text{ (Jmol}^{-1}\text{)}$
E_{AB}^{int}	$-1.24 \times 10^4 \text{ (Jmol}^{-1}\text{)}$	\mathbf{M}_A	$2.2 \times 10^{-19} \text{ (m}^2\text{s}^{-1}\text{J}^{-1}\text{)}$
θ	498(K)	\mathbf{M}_B	$2.2 \times 10^{-19} \text{ (m}^2\text{s}^{-1}\text{J}^{-1}\text{)}$

connected morphologies instead of the isolated islands like those in the 2D binary cases, as the three components have relatively the same concentrations (0.3, 0.3, 0.4), close to the off-critical point. The hydrostatic stress distribution is substantially inhomogeneous even inside the same phase due to the accompanying plastic deformation, as shown in figure 11(b). It can be seen that the magnitude of the hydrostatic stress only changes slightly during the phase coarsening stage, while the total plastic shear deformation increases gradually (figure 11(c)).

The corresponding 3D simulations of the ternary spinodal decomposition in the absence of mechanical deformation and only considering elastic deformation are presented in figure 12. Comparing figure 11(a) and figure 12, the separated phases produced by these three simulations exhibit qualitatively similar inter-connected morphologies. The approach of (Gameiro et al., 2005) could be used to quantify and distinguish the geometrical differences between these complicated patterns, however, the discussion is beyond the scope of the current work and represents work in progress to be reported on in the future.

5. Conclusions and Outlook

In this work, a numerical approach is pursued, using a semi-implicit convex splitting to invert the multi-component chemical potential relations, resulting in a numerically advantageous expression for their transport in terms of the chemical potential. The approach is validated using spinodal system as a benchmark. A convergence of the proposed weakly non-local approach to the strong CH form is demonstrated with increasing values of the penalty parameter. However, for prac-

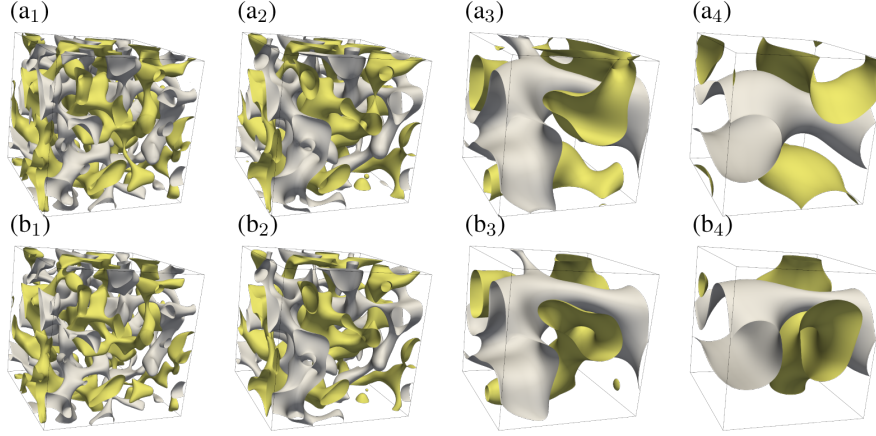


Figure 12: Evolution of the phase separation and coarsening in a ternary spinodal decomposition and coarsening process, (a) without mismatch solute strain, and (b) considering elastic deformation with a mismatch strain coefficient of $\nu_1 = 0.03\Omega$, at time (1) 400s, (2) 1000s, (3) 6000s, and (4) 15000s. The grey and yellow iso-surfaces represent (A-rich, B-poor) and (A-poor, B-rich) phases respectively, and the rest is (A-poor, B-poor) matrix phase. The concentrations of the iso-surfaces for both solute A and B are taken as 0.9.

tical purposes, a penalty parameter of $1 \times 10^5 \text{ Jmol}^{-1}$ was found to give sufficiently converged results. A significant reduction of the numerical cost and stability of the proposed approach is also demonstrated, allowing for the use of larger time steps in long-term diffusion simulations.

The influence of chemo-mechanical coupling, including both elastic and plastic deformation, on the phase separation and coarsening process is also investigated. It is found that the stored elastic energy can narrow the miscibility gap and alter the equilibrium concentrations for the separated phases. The phase separation kinetics is significantly reduced with increasing mismatch solute strain. Furthermore, the morphology of the solute-rich phase transitions from random droplet to ordered cubic due to the anisotropy of the elastic stiffness tensor. When considering plastic deformation in the case of realistic materials applications, it is observed that plasticity accounts for a significant amount of the dissipated elastic energy. The equilibrium concentration for separated phases are close to those in the absence of mechanical deformation, but the solute-rich phases tend to coalesce into elongated lamellar morphologies.

Extension of the proposed approach to multiphase systems is straightforward. This will be interesting as, in the context of multiphase systems, working directly

with the chemical potential lends itself naturally to the KKS description of interfaces (Kim et al., 1999), since no partitioning of the solute between phases is required. The proposed approach is also particularly amenable to CALPHAD-based descriptions of the chemical energy (Lukas et al., 2007), which is essential in the drive towards predictive simulations.

6. Acknowledgements

PS CL and BS gratefully acknowledge the financial support by the German Science Foundation (DFG) of the Priority Programme SPP 1713 "Strong Coupling of Thermo-chemical and Thermo-mechanical States in Applied Materials". PS is also grateful to the EPSRC for financial support through the associated programme grant LightFORM (EP/R001715/1) and the Airbus–University of Manchester Centre for Metallurgical Excellence for supporting aspects of this research.

7. References

References

- Balay, S., Abhyankar, S., Adams, M. F., Brown, J., Brune, P., Buschelman, K., Dalcin, L., Eijkhout, V., Gropp, W. D., Kaushik, D., Knepley, M. G., McInnes, L. C., Rupp, K., Smith, B. F., Zampini, S., Zhang, H., 2015. PETSc Users Manual.
- Barrett, J. W., Blowey, J. F., Garcke, H., 1999. Finite element approximation of the cahn–hilliard equation with degenerate mobility. *SIAM Journal on Numerical Analysis* 37 (1), 286–318.
- Boettinger, W. J., Warren, J. A., Beckermann, C., Karma, A., 2002. Phase-field simulation of solidification. *Annual review of materials research* 32 (1), 163–194.
- Boyer, F., Minjeaud, S., 2011. Numerical schemes for a three component Cahn–Hilliard model. *ESIAM Journal of Mathematical Modeling and Numerical Analysis* 45, 697–738.
- Cahn, J. W., Hilliard, J. E., 1958. Free energy of a non-uniform system. I. Interfacial energy. *Journal of Chemical Physics* 28, 258–267.

- Choudhury, A., Nestler, B., 2012. Grand-potential formulation for multicomponent phase transformations combined with thin-interface asymptotics of the double-obstacle potential. *Phys. Rev. E* 85, 021602.
- de Groot, S., Mazur, P., 1962. *Non-Equilibrium Thermodynamics*. North Holland Publishers, Amsterdam.
- Elliott, C. M., Stuart, A. M., 1993. The global dynamics of discrete semilinear parabolic equations. *SIAM Journal of Numerical Analysis* 30, 1622–1663.
- Emmerich, H., 2008. Advances of and by phase-field modelling in condensed-matter physics. *Advances in Physics* 57 (1), 1–87.
- Eyre, D. J., 1998. Unconditionally gradient stable time marching the Cahn-Hilliard equation. In: *Computational & Mathematical Models of Microstructural Evolution (Symposium BB)*. Vol. 529. MRS Proceedings, pp. 39–46.
- Furihata, D., 2001. A stable and conservative finite difference scheme for the cahn-hilliard equation. *Numerische Mathematik* 87 (4), 675–699.
- Gameiro, M., Mischaikow, K., Wanner, T., 2005. Evolution of pattern complexity in the cahn-hilliard theory of phase separation. *Acta Materialia* 53 (3), 693–704.
- Gladkov, S., Svendsen, B., 2015. Thermodynamic and rate variational formulation of models for inhomogeneous gradient materials with microstructure and application to phase field modeling. *Acta Mechanica Sinica* 31 (2), 162–172.
- Gomez, H., Calo, V. M., Bazilevs, Y., Hughes, T. J., 2008. Isogeometric analysis of the cahnhilliard phase-field model. *Computer Methods in Applied Mechanics and Engineering* 197 (49), 4333 – 4352.
- Gomez, H., Hughes, T. J. R., 2011. Provably unconditionally stable, second-order time-accurate, mixed variational methods for phase-field models. *Journal of Computational Physics* 230, 5310–5327.
- Hüter, C., Shanthraj, P., McEniry, E., Spatschek, R., Hickel, T., Tehranchi, A., Guo, X., Roters, F., 2018. Multiscale modelling of hydrogen transport and segregation in polycrystalline steels. *Metals* 8 (6), 430.

- Jokisaari, A. M., Naghavi, S. S., Wolverton, C., Voorhees, P. W., Heinonen, O. G., 2017. Predicting the morphologies of γ' precipitates in cobalt-based superalloys. *Acta Materialia* 141, 273–284.
- Kim, S. G., Kim, W. T., Suzuki, T., Dec 1999. Phase-field model for binary alloys. *Phys. Rev. E* 60, 7186–7197.
URL <https://link.aps.org/doi/10.1103/PhysRevE.60.7186>
- Kontis, P., Li, Z., Collins, D. M., Cormier, J., Raabe, D., Gault, B., 2018. The effect of chromium and cobalt segregation at dislocations on nickel-based superalloys. *Scripta Materialia* 145, 76–80.
- Korbmacher, D., von Pezold, J., Brinckmann, S., Neugebauer, J., Hüter, C., Spatschek, R., 2018. Modeling of phase equilibria in ni-h: Bridging the atomistic with the continuum scale. *Metals* 8 (4), 280.
- Liu, C., Shanthraj, P., Diehl, M., Roters, F., Dong, S., Dong, J., Ding, W., Raabe, D., 2018. An integrated crystal plasticity–phase field model for spatially resolved twin nucleation, propagation, and growth in hexagonal materials. *International Journal of Plasticity* 106, 203–227.
- Lukas, H., Fries, S. G., Sundman, B., 2007. Computational thermodynamics: the Calphad method. Cambridge university press.
- Mianroodi, J. R., Shanthraj, P., Kontis, P., Cormier, J., Gault, B., Svendsen, B., Raabe, D., 2019. Atomistic phase field chemomechanical modeling of dislocation-solute-precipitate interaction in ni-al-co. *Acta Materialia*.
- Miehe, C., 2011. A multi-field incremental variational framework for gradient-extended standard dissipative solids. *Journal of the Mechanics and Physics of Solids* 59, 898–923.
- Miehe, C., 2014. Variational gradient plasticity at finite strains. Part I: Mixed potentials for the evolution and update problems of gradient-extended dissipative solids. *Computer Methods in Applied Mechanics and Engineering* 268, 677–703.
- Moelans, N., Blanpain, B., Wollants, P., 2008. An introduction to phase-field modeling of microstructure evolution. *Calphad* 32 (2), 268–294.

- Nestler, B., Wheeler, A., 2000. A multi-phase-field model of eutectic and peritectic alloys: numerical simulation of growth structures. *Physica D: Nonlinear Phenomena* 138 (1), 114–133.
- Peirce, D., Asaro, R., Needleman, A., 1983. Material rate dependence and localized deformation in crystalline solids. *Acta Metallurgica* 31 (12), 1951 – 1976.
- Plapp, M., 2011. Unified derivation of phase-field models for alloy solidification from a grand-potential functional. *Physical Review E* 84, 031601.
- Roters, F., Diehl, M., Shanthraj, P., Eisenlohr, P., Reuber, C., Wong, S. L., Maiti, T., Ebrahimi, A., Hochrainer, T., Fabritius, H.-O., et al., 2019. Damask—the düsseldorf advanced material simulation kit for modeling multi-physics crystal plasticity, thermal, and damage phenomena from the single crystal up to the component scale. *Computational Materials Science* 158, 420–478.
- Roters, F., Eisenlohr, P., Hantcherli, L., Tjahjanto, D., Bieler, T., Raabe, D., 2010. Overview of constitutive laws, kinematics, homogenization and multi-scale methods in crystal plasticity finite-element modeling: Theory, experiments, applications. *Acta Materialia* 58 (4), 1152 – 1211.
- Sagiyama, K., Rudrarajua, S., Garikipati, K., 2016. Unconditionally stable, second-order accurate schemes for solid state phase transformations driven by mechano-chemical spinodal decomposition. *Computer Methods in Applied Mechanics and Engineering* 311, 556–575.
- Schneider, D., Schoof, E., Huang, Y., Selzer, M., Nestler, B., 2017. Phase-field modeling of crack propagation in multiphase systems. *Computer Methods in Applied Mechanics and Engineering* 312, 186–195.
- Schwarze, C., Gupta, A., Hickel, T., R., D. K., 2017. Phase-field study of ripening and rearrangement of precipitates under chemomechanical coupling. *Physical Review B* 95, 174101.
- Shanthraj, P., Sharma, L., Svendsen, B., Roters, F., Raabe, D., 2016. A phase field model for damage in elasto-viscoplastic materials. *Computer Methods in Applied Mechanics and Engineering* 312, 167–185.
- Shanthraj, P., Svendsen, B., Sharma, L., Roters, F., Raabe, D., 2017. Elasto-viscoplastic phase field modelling of anisotropic cleavage fracture. *Journal of the Mechanics and Physics of Solids* 99, 19–34.

- Shanthraj, P., Zikry, M., 2011. Dislocation density evolution and interactions in crystalline materials. *Acta materialia* 59 (20), 7695–7702.
- Shanthraj, P., Zikry, M., 2012. Optimal microstructures for martensitic steels. *Journal of Materials Research* 27 (12), 1598–1611.
- Svendsen, B., 2004. On the thermodynamic- and variational-based formulation of models for inelastic continua with internal lengthscales. *Computer Methods in Applied Mechanics and Engineering* 48, 5429–5452.
- Tavakoli, R., 2016. Unconditionally energy stable time stepping scheme for Cahn-Morral equation: application to multi-component spinodal decomposition and optimal space tiling. *Journal of Computational Physics* 304, 441–464.
- Ubachs, R. L. J. M., Schreurs, P. J. G., Geers, M. G. D., 2004. Microstructure evolution of tin-lead solder. *IEEE Transactions on Components and Packaging Technologies* 27 (4), 635–642.
- Vaithyanathan, V., Chen, L. Q., 2002. Coarsening of ordered intermetallic precipitates with coherency stress. *Acta Materialia* 50 (16), 4061–4073.
- Wu, Q., Shanthraj, P., Zikry, M., 2014. Modeling the heterogeneous effects of retained austenite on the behavior of martensitic high strength steels, 241–252.
- Zhou, N., Shen, C., Mills, M., Wang, Y., 2010. Large-scale three-dimensional phase field simulation of γ' -rafting and creep deformation. *Philosophical Magazine* 90 (1-4), 405–436.
- Zhu, J., Chen, L.-Q., Shen, J., Tikare, V., 1999. Coarsening kinetics from a variable-mobility cahn-hilliard equation: Application of a semi-implicit fourier spectral method. *Phys. Rev. E* 60, 3564–3572.